LARGE-AREA MAPPING AT 850 MICRONS. I. OPTIMUM IMAGE RECONSTRUCTION FROM CHOP MEASUREMENTS

DOUG JOHNSTONE,[1] CHRISTINE D. WILSON,[2] GERALD MORIARTY-SCHIEVEN,[3]
JEAN GIANNAKOPOULOU-CREIGHTON,[4] AND ERIK GREGERSEN[2]

ABSTRACT

We present results on the optimum reconstruction of chop data taken using the Submillimeter Common-User Bolometer Array on the James Clerk Maxwell Telescope. Using an artificial data set with known noise properties, we analyze three techniques for constructing images of the sky from the chop data: Emerson Fourier deconvolution, matrix inversion, and maximum entropy reconstruction. We conclude that a matrix inversion formulation via an iterative procedure produces the best image reconstructions. We apply the three reconstruction techniques to produce maps of the calibration point source CRL 618 and the ρ Ophiuchi A core at 850 μm and use Wiener filtering to remove the high-frequency noise component from the matrix inversion method.

Subject headings: infrared: ISM: continuum — ISM: structure — methods: data analysis — submillimeter

1. INTRODUCTION

Technological improvements in submillimeter instrumentation over the last few years have enabled astronomers to map large (hundreds of square arcminutes) areas of star-forming regions (Motte, André, & Neri 1998; Johnstone & Bally 1999; Wilson et al. 1999) with reasonable resolution (8″–14″ beams) and high sensitivity (rms noise ∼ 0.01 Jy beam^{-1}). While the capability of submillimeter instruments has improved dramatically (Holland et al. 1999), removing the interference produced at submillimeter wavelengths by the rapidly varying atmosphere of Earth still requires complex chopping procedures during the measurement process at the telescope. Instead of taking individual flux measurements at each position on the sky, difference measurements are taken between two locations separated by a chop distance and direction. By taking these difference measurements quickly, usually at a rate of several hertz, the foreground atmosphere is effectively frozen in time, and the signal provides a direct measure of the difference in flux between the two locations within the molecular cloud. Producing a flux map of the molecular cloud from a set of difference measurements requires deconvolving the chop beam, careful consideration of the sources of noise during the observations, and an understanding of the propagation of these uncertainties through the reconstruction technique.

Many techniques for reconstructing an image of the sky from such chop maps have been proposed including Fourier deconvolution (Emerson, Klein, & Haslam 1979; Emerson 1995), maximum entropy (Richer 1992; Wilson et al. 1999), and other nonlinear methods such as Pixon reconstruction (Jenness et al. 2000). Cosmologists, anticipating significant advances in satellite observations of the cosmic microwave background, have also considered matrix inversion solutions to reconstruct images from chop maps (Wright, Hinshaw, & Bennett 1996). However, only a limited number of comparative tests have been performed to analyze the strengths and weaknesses of each individual technique (see, for example, Richer 1992). This paper analyzes three techniques for making maps: Fourier deconvolution, matrix inversion, and maximum entropy reconstruction (although the maximum entropy construction used in this paper is fundamentally different from that used by Richer 1992). We define the optimal image reconstruction algorithm as one that reproduces the original image most exactly in the absence of noise (minimum χ^2) and that accounts properly for any variation in the noise across the map due to changes in the measurement uncertainty. An efficient procedure is one that requires few calculations to produce a reliable map; the variances in the final map may be higher than produced by the optimal map reconstruction algorithm, but the technique neither preferentially removes structure nor introduces spurious sources.

The standard SURF software (Jenness & Lightfoot 1999) for reduction of James Clerk Maxwell Telescope (JCMT) data includes a Fourier deconvolution routine for image reconstruction following the formulation of Emerson (1995), an expansion on the method introduced by Emerson et al. (1979). By holding the chop distance and chop direction fixed with respect to the sky in producing a difference map, the chop itself can be considered a simple convolution of the sky with both a positive and negative delta function separated by the chop distance λ_0. Thus, if S is the sky and C is the dual delta-function chop profile, then the difference observation of the sky, D, is

$$D = S \otimes C, \qquad (1)$$

where $\otimes$ represents a convolution. The Fourier transform, $c(\lambda)$, of the dual delta-function is particularly simple, containing only an imaginary component:

$$c(\lambda) = i \sin\left(\frac{\lambda_0}{\lambda}\pi\right). \qquad (2)$$

Recognizing that since a convolution in physical space is identical to a multiplication in Fourier space, one can simply reconstruct chop maps as follows: one deconvolves

[1] Department of Astronomy, University of Toronto, Toronto, ON, M5S 3H8, Canada; johnstone@astro.utoronto.ca.
[2] Department of Physics and Astronomy, McMaster University, Hamilton, ON, L8S 4M1, Canada.
[3] National Research Council of Canada, Joint Astronomy Center, 660 North Aohoku Place, University Park, HI, 96720.
[4] Infrared Processing and Analysis Center, Jet Propulsion Laboratory, California Institute of Technology, Pasadena CA 91125.

the chop by transforming the difference data into the Fourier domain, divides out the Fourier transform of the dual delta-function, and then performs an inverse Fourier transformation back to real space. However, the presence of nulls in the sine function in equation (2) produces unsatisfactory results for Fourier modes with spatial frequencies equal to, or at integer multiples of, the chop distance. Thus, these frequencies, and their immediate neighbors, are usually removed from the resultant map. By obtaining more than one chop map at the telescope, the Emerson (1995) technique reduces this constraint and allows for a complete Fourier deconvolution reconstruction up to the lowest frequency that is an integer multiple of all chop distance spatial frequencies. For the typical $20''$, $30''$, $65''$ chop distances used at the JCMT, the first indeterminable wavelength is $5''$, smaller than both the $8''$ beam at 450 μm and $14''$ beam at 850 μm obtained at the telescope.

For very long wavelength modes, $\lambda \gg \lambda_0$, the convolution function decays rapidly, $c \propto 1/\lambda$, and thus the signal obtained in the difference maps for these wavelengths is considerably diminished. Reconstruction of the signal requires an extreme amplification, essentially division by c. The addition of Gaussian random noise to the chopped data adds a flat power spectrum component, with equal amplitude at *all* wavelengths since the noise is uncorrelated in space. Thus, image reconstruction will amplify the long-wavelength component associated with this noise. This is an unavoidable consequence of chopping; the long-wavelength signal will always be diminished with respect to any random noise component regardless of the manner in which the reconstruction is attempted. More details on Emerson Fourier deconvolution including detailed comparisons between the two versions can be found in Emerson (1995) and Jenness, Lightfoot, & Holland (1998).

Maximum entropy has been used to reproduce scan-maps taken with the JCMT (Wilson et al. 1999) and is therefore included in this analysis. The maximum entropy reconstruction that we test mimics interferometric techniques by producing a synthetic beam from the chop data. We then use a standard implementation of the maximum entropy algorithm to reconstruct images of the sky. While the base technique is the same as that used by Richer (1992), in this paper we do not test his adaptation. Maximum entropy reconstruction is based on the assumption that, given a choice, the most likely reconstruction is that one that maximizes a given entropy law. The observations, together with a knowledge of the noise, are used to constrain the possible map reconstructions. Maximum entropy (see Narayan & Nityananda 1986 for a review) has been very successful in producing images of the sky in severely undersampled domains, such as interferometric observations in which only a fraction of the Fourier components are measured. In these regimes, some assumption about the unsampled signal components is required in order to reconstruct the image. Our scan-maps produce severely *oversampled* data, and, in the absence of noise, image reconstruction should be exact. We note that in our map reconstructions there is no attempt to deconvolve the finite beam of the telescope; we are only attempting to remove the chop pattern.

In its standard implementation, the maximum entropy image reconstruction method is not well suited to reconstructing chop data. First, the total flux in the map is a significant constraint used by maximum entropy techniques, but this is the one number that is *not* obtained by the two-point chop data acquisition. Without the constraint, the total flux in the final map depends sensitively on the assumed rms noise level. Second, maximum entropy techniques require that the sky brightness be positive definite everywhere; however, since the total flux in the map is unknown, there may exist regions with negative relative brightness. Finally, many maximum entropy implementations attempt to determine the level of the noise during the reconstruction. Since negative features are not allowed to be signal, they are instead assumed to be noise. Thus, the noise is overestimated, reducing the constraint each measurement makes. The maximum entropy law employed attempts to produce the flattest map possible given the constraints. If the total flux in the region is the only known quantity, the maximum entropy image reconstruction is a constant surface brightness map. In treating negative features as noise, the maximum entropy image reconstruction tends to overcompensate and produces a flatter map than it should.

In § 2 we develop an iterative method for matrix inversion image reconstruction for chop data taken with the JCMT, following the formulation of Wright et al. (1996). We use artificial data sets to test the three different techniques for creating images from chop data in § 3 and determine that the computationally expensive iterative method for matrix inversion produces the most accurate reconstruction with a quantifiable measure of the variance at each location in the final map. Section 4 considers the addition of correlated noises to the image reconstruction problem and applies the three techniques to real data taken with the JCMT at 850 μm. In addition, Wiener filtering is applied to remove the high spatial frequency component of the noise from the matrix inversion reconstruction. The paper is summarized in § 5. A companion paper (Johnstone et al. 2000, hereafter Paper II) applies the matrix inversion technique to a large-area 850 μm map of the ρ Ophiuchi molecular cloud and discusses the clump mass function and two-point correlation function.

2. MATRIX INVERSION

One limitation of Emerson Fourier deconvolution is that, at present, there is no method within this technique for weighting sections of the input maps properly for known variations in the noise component. For example, the noise is often different for each bolometer in the detector array, and thus the noise in the resultant chop map depends on which bolometers covered each segment of the sky. Also, if extra observing time is spent on one portion of the map, the noise in that section should be lower. Significant weather changes during an observing run can also produce variations in the noise with location in the chop maps. If the noise component is Gaussian random and can be determined, i.e., the noise component is measurable from the observations, then there exist optimal image reconstruction algorithms that utilize each individual chop measurement and its associated uncertainty independently.

The matrix inversion image reconstruction proceeds as follows. We partition the imaged sky into a regular grid at the required sampling spacing such that there are M cells in width and N cells in length (for JCMT measurements, one usually uses $3''$ cells to provide subsampling of the $8''$ beam at 450 μm; thus a $768'' \times 768''$ field contains $M = N = 256$ cells in each direction). Each cell is then labeled with a unique integer between 1 and $M \times N$, and the brightness of

the sky in all the cells can be written as a vector S with $M \times N$ unique elements. The difference measurements (the observed chop measurements on the sky) can be written as a vector D with I elements, where I equals the total number of chop measurements obtained at the telescope (in practice, each $768'' \times 768''$ scan-map made at the JCMT contains $I \sim 10^6$ difference measurements on a grid of $M \times N \sim 10^5$ elements for an *oversampling* factor of 10). Any individual single chop can be described by a vector with length $M \times N$, and all elements are zero except for a value of $+1$ at the positive measurement location on the sky and a value of -1 at the negative measurement location (different chop procedures could be used, such as central differencing, which would require only slight modifications in the location and values of the nonzero elements within the vector). The collection of chops produces a matrix C with $M \times N$ elements across and I elements in length. In the absence of noise,

$$D = CS ,$$ (3)

and matrix inversion allows for recovery of the sky brightness S from the observed difference measurements D and the chop configuration C.

The matrix C typically contains 10^{11} elements of which all but $\sim 10^6$ are zeros but which is nevertheless nontrivial to invert unless the matrix has a very regular structure such as being bidiagonal. The Emerson Fourier deconvolution is in essence an efficient matrix inversion routine for a set of bidiagonal matrices. The addition of noise further complicates matters. Assuming the noise in each measurement is strictly random then the noise vector N (with I elements) must be added to equation (3), to give

$$D = CS + N ,$$ (4)

where each element of N need not be drawn from the same Gaussian distribution.

Cosmologists, in preparing for data sets with similar sized matrices, have spent considerable effort in obtaining optimal and efficient methods for determining S from equation (4) and have found that an iterative scheme works extremely well and converges quickly (Wright et al. 1996). The iterative scheme assumes an initial solution S', usually taken to be a blank image, for S. A new value for each element is then calculated using the difference between the measured vector D and the vector D' obtained from S' and equation (3). The measurements are also weighted by the known variance σ in each measurement. For two-point chops such as those used at the JCMT, the updated map S'' is given by

$$S_i'' = \frac{\sum_t [(\delta_{i,p(t)}/\sigma_t^2)(S'_{m(t)} + D_t) + (\delta_{i,m(t)}/\sigma_t^2)(S'_{p(t)} - D_t)]}{\sum_t [(\delta_{i,p(t)}/\sigma_t^2) + (\delta_{i,m(t)}/\sigma_t^2)]} .$$

(5)

In equation (5), the subscripts refer to the element within the vector; $p(t)$ is spatial location of the positive measurement for chop t, and $m(t)$ is spatial location of the negative measurement for chop t. Each observed difference measurement is applied against the guessed map to produce a weighted update for each cell and a more accurate map. The resulting vector S'' is then used to replace S' with iteration continuing until convergence.

Convergence is quick for short-wavelength modes but takes considerable time for long-wavelength modes, as the coupled information across many chops must be combined. The number of iterations required scales quadratically with the longest length across the map and as the inverse square of the longest chop distance. (Strictly speaking, maximal convergence requires using the shortest chop throw; however, in practice the relative convergence of the map diminishes significantly once the longest chop throws have converged across the full map.) For a map of length $768''$ ($256'' \times 3''$) and with a largest chop of $65''$, approximately 100 iterations are required. The number of calculations for each iteration grows *linearly* with the number of difference measurements.

3. TESTING TECHNIQUES WITH ARTIFICIAL DATA

To test the general applicability of the three reconstruction algorithms discussed above, we produced an artificial image with both wave components and Gaussian peaks. The features chosen for the artificial image are designed to simulate both large-scale features and localized structures within the ISM, and any image reconstruction technique should be capable of reproducing both components equally well. The artificial image is shown in Figure 1. The map covers an area of $768'' \times 768''$ and is sampled with $3''$ spacing. It consists of four waves with amplitudes ranging from 0.1 to 0.2 Jy and with wavelengths $50''-650''$ and random orientation. Four Gaussian sources were added to the map with peak brightnesses ranging from 0.1 to 3.0 Jy and with widths $\sigma = 10''-50''$. Only the two brightest Gaussian sources are easily visible in Figure 1.

The image was chopped to simulate the typical observing procedure used at the JCMT. The map was chopped in a regular manner, with difference measurements taken along the horizontal and vertical directions with $20''$, $30''$, and $65''$ spacings, which simulates data taken chopping in right ascension and declination. For difference measurements at the edge of the map, the wave and Gaussian structures were assumed to continue beyond the image boundary. To simulate real observations, Gaussian random noise was added to the difference measurements either uniformly across the map or with a larger noise for differences obtained in the lower left-hand quadrant. The same chopped difference measurements and noises were used to test all three image reconstruction algorithms. Changing sky conditions during observations with the JCMT also introduce $1/f$-noise, which produces correlated spatial variations, especially on large scales. However, defining and removing this noise component is much trickier. Since the uncertainties associated with these effects are much less than the Gaussian random fluctuations associated with each individual chop measurement, correlated noises are dealt with as secondary effects when analyzing real data (see § 4).

Five map reconstructions were performed for each technique: (1) reconstruction of the artificial image from the chop data with no noise; (2) reconstruction of the artificial image from the chop data with uniformly weighted noise; (3) reconstruction of a blank image with the same uniform noise; (4) reconstruction of the artificial image from the chop data with nonuniform noise (described below); and (5) reconstruction of a blank image with the same nonuniform noise. The resulting maps were then compared with the original artificial image and with each other. The results show that matrix inversion is the optimal reconstruction, method while the Fourier deconvolution is efficient, producing reliable maps under most conditions.
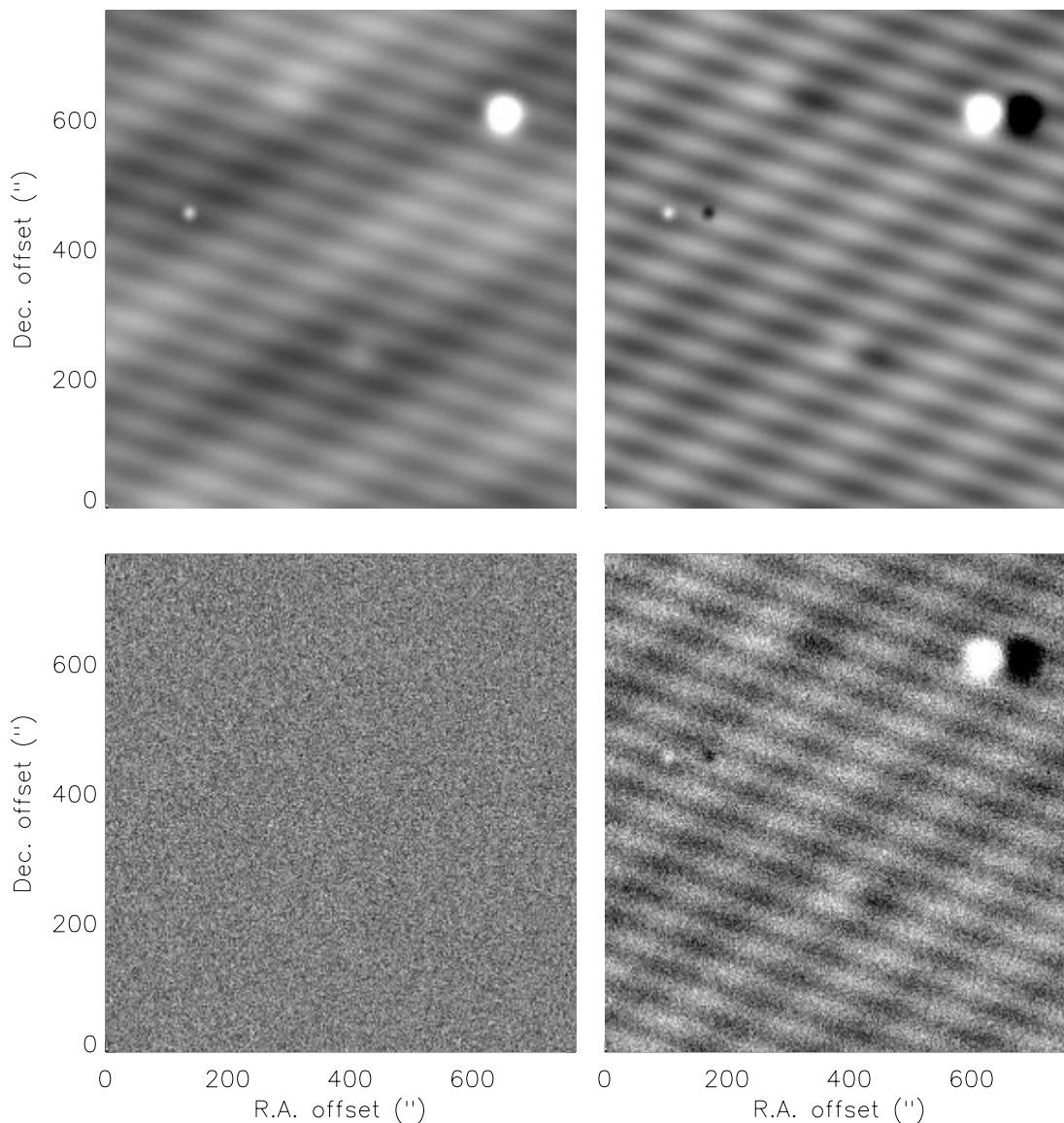
FIG. 1.—Artificial map produced for comparing image reconstruction techniques (*upper left*) along with three maps chopped at 65″ horizontally: artificial map chopped without noise (*upper right*); artificial map chopped with added noise (*lower right*); and blank sky map chopped with added noise (*lower left*). For all maps the intensity scale is -1.0 to 1.0 Jy beam^{-1}.

3.1. *Emerson Fourier Deconvolution*

The Emerson Fourier deconvolution reconstruction provided by the JCMT with the standard data analysis software is powerful, efficient, and produces reliable fits to the artificial data (Fig. 2). The technique suffers from significant edge residuals owing to the use of fast Fourier transforms, which assume that edges of the image region wrap cleanly. When no noise is added to the chop maps, the central quarter of the image reconstruction shows little difference from the original data. When uniformly distributed Gaussian random noise is added, the central region becomes noisier but shows no systematic effects with location. Reconstructing the noise and the signal data separately and then summing the result reproduces exactly the image reconstruction of the signal and noise together. This linearly additive feature of the reconstruction allows us to test the signal and noise propagation properties independently from each other. It also removes any concern over the applicability of the artificial input map used to test the image recon-

struction technique since the linearity of the reconstruction allows for producing any image through a combination of individual component maps.

3.2. *Matrix Inversion*

Figure 3 shows the image reconstruction capabilities of matrix inversion by iteration. Unlike the Emerson technique, there are no obvious edge effects, and the difference map between the reconstructed map and the original artificial image is much flatter. Figure 3 also shows that the matrix inversion reconstruction is a linear method; reconstructing the noise and signal separately and combining the result is identical to reconstructing the noise and signal together. The full benefit of the matrix inversion technique is obtained when the noise in the map is not uniform. As mentioned above, the Emerson Fourier deconvolution does not allow independent weighting for each measurement. To test the improvement possible with the matrix iteration technique, we produced difference maps with noise added
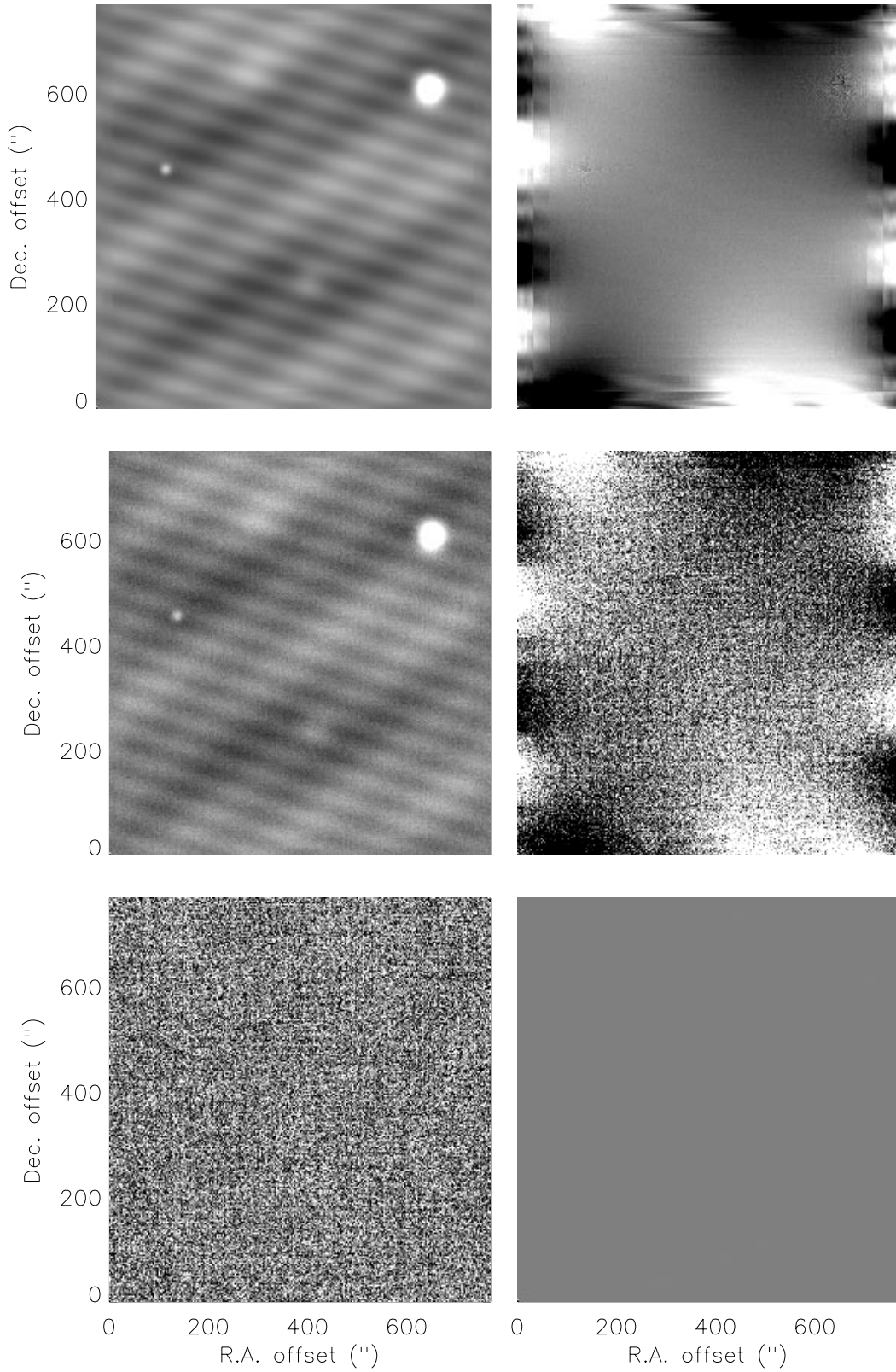
FIG. 2.—Reconstruction of image in Fig. 1 using the Emerson Fourier deconvolution. *Top row*: Reconstruction from chop maps without noise (*left*) and difference between the reconstructed map and the original artificial map (*right*). *Middle row*: Reconstruction from chop maps with uniform noise (*left*) and difference between the reconstructed map and the original artificial map (*right*). *Bottom row*: Reconstruction from chop maps containing *only* uniform noise and no signal (*left*) and the difference between the sum of the top plus bottom map reconstructions and the middle map reconstruction (*right*). The intensity scale for the top left-hand and middle left-hand panels is -1.0 to 1.0 Jy beam^{-1}, while the rest of the panels have an intensity scale -0.1 to 0.1 Jy beam^{-1}.
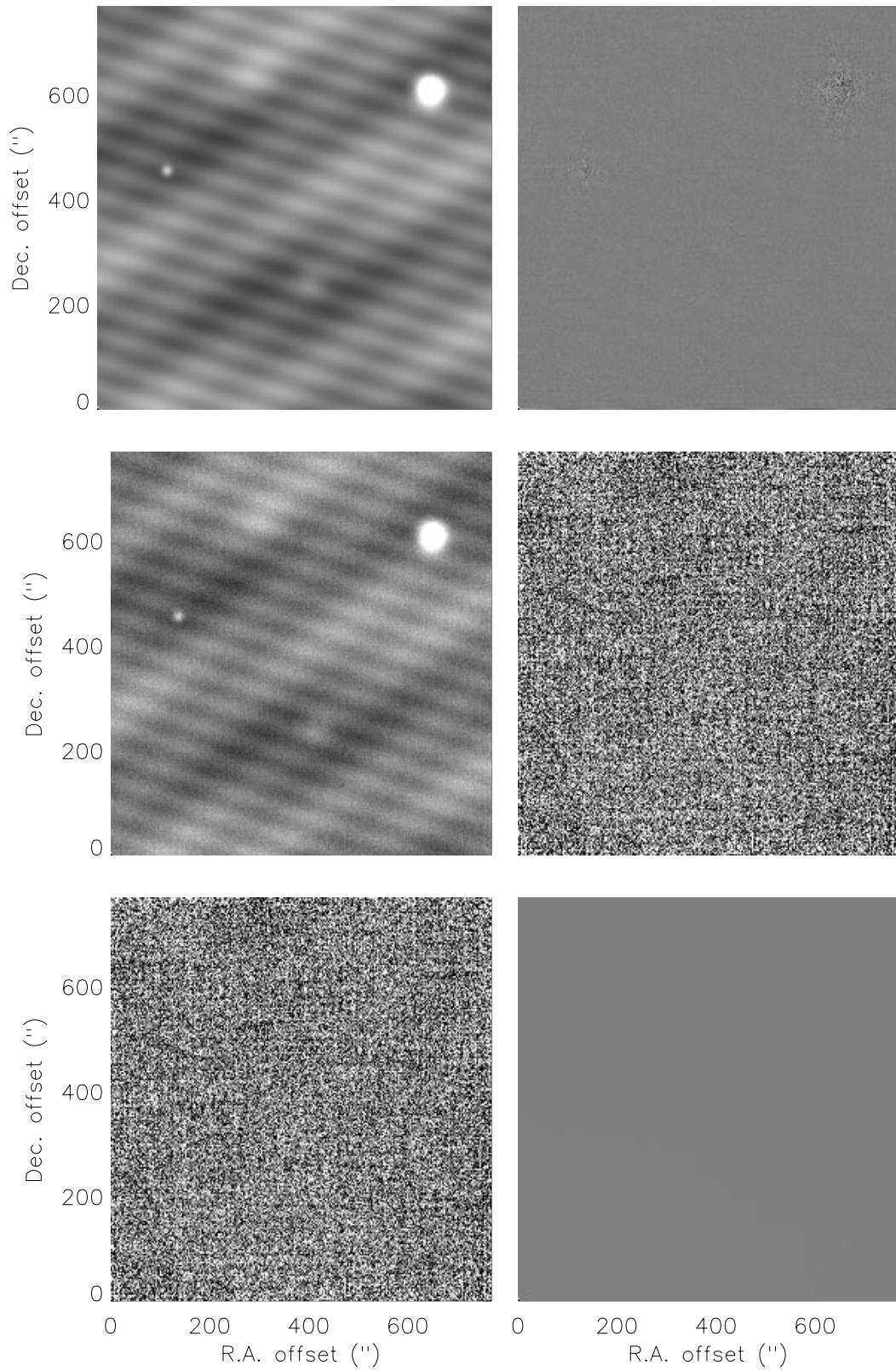
Fig. 3.—Reconstruction of image in Fig. 1 using the iterative matrix inversion technique. *Top row*: Reconstruction from chop maps without noise (*left*) and difference between the reconstructed map and the original artificial map (*right*). *Middle row*: Reconstruction from chop maps with uniform noise (*left*) and difference between the reconstructed map and the original artificial map (*right*). *Bottom row*: Reconstruction from chop maps containing *only* uniform noise and no signal (*left*) and the difference between the sum of the top plus bottom map reconstructions and the middle map reconstruction (*right*). The intensity scales are the same as in Fig. 2.
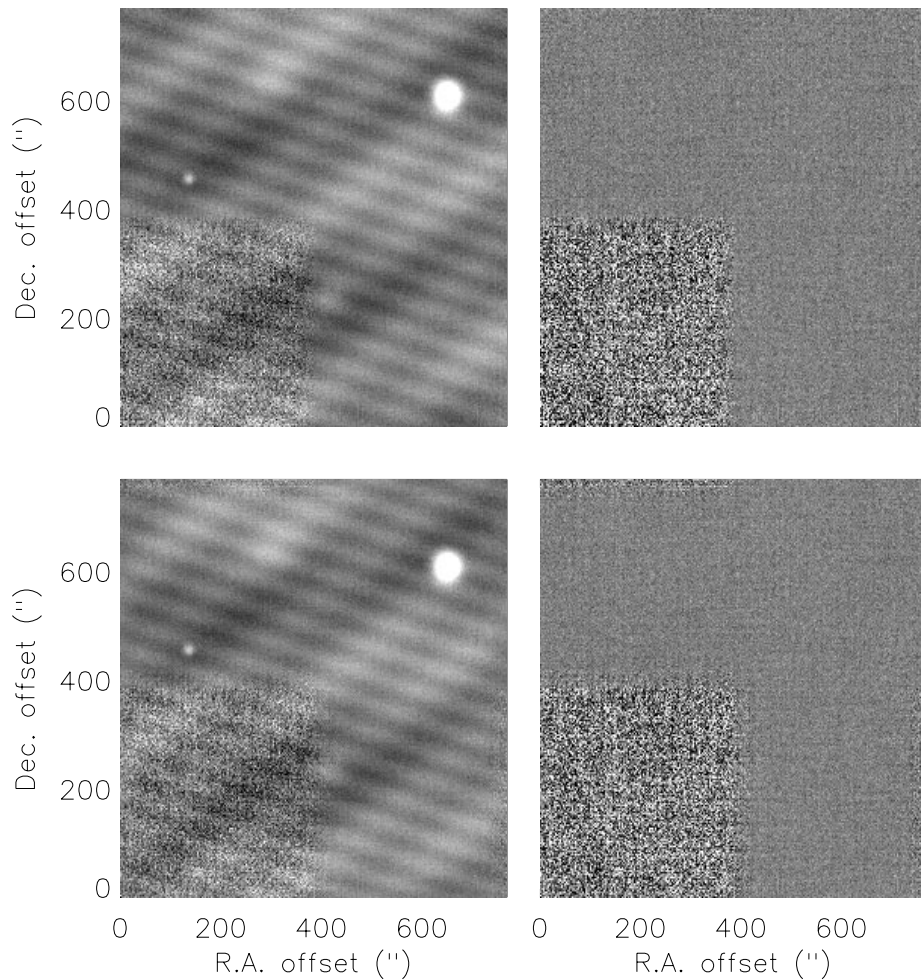
FIG. 4.—Reconstruction when the noise is not uniform across the image (*top row*) using the iterative matrix inversion technique from chop maps of the artificial data (Fig. 1) with nonuniform noise (*left*) and from chop maps of a blank sky with the same nonuniform noise (*right*). *Bottom row*: Reconstruction using the Emerson Fourier deconvolution technique from chop maps of the artificial data with nonuniform noise (*left*) and from chop maps of a blank sky with the same nonuniform noise (*right*). Note that the Emerson Fourier deconvolution spreads the region containing higher noise. The intensity scales are -1.0 to 1.0 Jy beam^{-1} for the left-hand column and -0.5 to 0.5 Jy beam^{-1} for the right-hand column.

nonuniformly such that one quadrant of the image had five times the level of noise as the rest of the map. The reconstructed maps are shown in Figure 4. Careful examination reveals that the Emerson Fourier reconstruction spreads the noise outward from the lower left-hand quadrant.

A quantitative test was performed in order to verify the capabilities of the matrix inversion technique by reconstructing a blank sky image of the nonuniform noise map without any added signal. Figure 5 plots the variance in both the Emerson Fourier deconvolution reconstruction and the matrix inversion reconstruction along the horizontal direction in the map after summing vertically across the first 100 pixels. As expected, the variance is 5 times larger over the first half of the map; however, the matrix inversion technique confines the variance to the first half alone, while the Emerson Fourier deconvolution spreads the enhanced variance into the intrinsically less noisy region.

3.3. *Maximum Entropy Reconstruction*

In reconstructing the artificial image using the maximum entropy method, there was no modification to the synthetic beam technique supplied with the MIRIAD (Sault, Teuben, & Wright 1995) software package. The individual chop

maps produced in the manner described above were summed together as by Wilson et al. (1999) to produce a single map with a well-defined synthetic beam represented by one positive peak at the center (with amplitude $+1$) and 12 negative peaks symmetrically about the center (with amplitude $-1/12$). (Note that Wilson et al. 1999 used an asymmetric beam, while we have used a symmetrized version of the method by summing both the chopped maps and the inverse of the chopped maps, each shifted appropriately in right ascension and declination so that the positive signals for a given source add together.) Each of the artificial maps discussed above were reconstructed, and the results are shown in Figure 6. The results are particularly poor because the input map consists of both waves and Gaussian profiles. Even when no noise is added, the maximum entropy reconstruction has trouble accounting for the low-amplitude long-wavelength modes. Instead of reproducing the input map, the maximum entropy technique determines that the long-wavelength features are simply noise and produces a flatter map with only a few peaks. Note that the residual properties of the resultant maps are *not* random. Maximum entropy does not attempt to constrain the noise to be spatially white. Given that
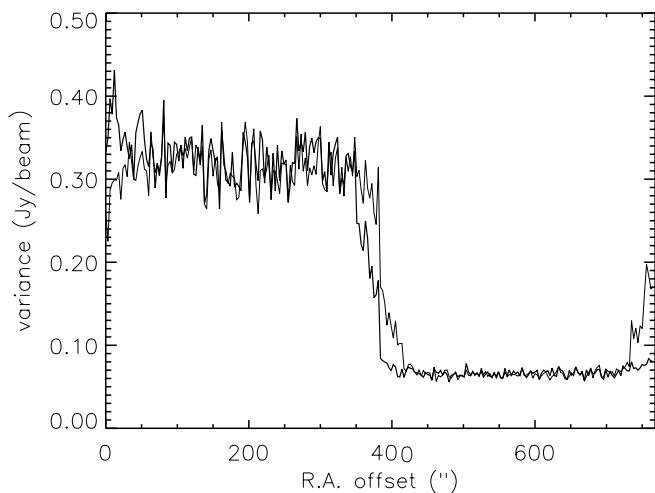
FIG. 5.—Computation of the variance as a function of horizontal position across the first 100 pixels (vertically) in the residual maps of Fig. 4. Note that the noise was amplified by a factor of 5 in the first quadrant (*first half of the plot*). The thin line denotes the variance measured from the residual in the Emerson Fourier deconvolution. The thick line denotes the variance measured from the residual in the iterative matrix inversion technique. Note that the Emerson reconstruction shows a severe increase in variance at the right edge, as well as a slower drop across the transition from the high noise to the low noise quadrant.

the long-wavelength modes have been removed during the reconstruction, there exist large regions in which the residuals are entirely negative or positive.

3.4. *Comparing the Three Techniques*

The above analysis shows that the matrix inversion technique produces the optimal map. The Emerson Fourier deconvolution is an efficient algorithm but suffers edge effects and diffusion when the noise is nonuniform. The standard implementations for synthetic beam maximum entropy reconstruction require as input a target rms noise level for the map, which is used to determine when the algorithm has converged and which has a large influence on the total flux in the final map. During reconstruction, these noise properties are determined such that the map is positive definite everywhere, a poor assumption given the lack of knowledge for the total flux. Given the severe oversampling of data (factor of 10 at least), we assume that the noise characteristics of the individual bolometers and of the changing sky can be determined with sufficient accuracy, and thus we suggest that matrix inversion techniques such as the iterative method described above are optimal. The Emerson Fourier deconvolution can certainly be used to produce adequate maps quickly, particularly when structure at the map edge can be ignored *and* when variability in the noise across the map is not important.

The tests show that optimal reconstruction is obtained by utilizing *all* information available. Calculating the matrix inversion reconstruction of the artificial maps requires about 5 minutes on a Pentium III Linux computer, while the Emerson Fourier deconvolution requires only a fraction of a minute. The iterative procedure requires many more computations than the Emerson method for two reasons: (1) each difference measurement is treated individually with an individual noise component rather than as part of a convolved map of the sky with assumed uniform noise, and (2) no specific form of the chopping geometry is assumed.

The increase in the reliability of the reconstructed image outweighs the increase in computations and computer time required to perform the calculation; on a dedicated computer of modest power, the time required to produce reconstructions of square degree fields is only tens of hours. Maximum entropy reconstruction of similar sized fields requires a few hours of computer time and cannot be fully automated, as it requires a person to inspect the results periodically and work interactively with the computer on the reduction.

When using the matrix inversion technique, the chopping strategy used at the telescope should be determined such that the systematic uncertainties inherent in the observations are reduced. One method used successfully to reduce the effects of baseline offset, where the difference measurements are slightly offset by either a constant or linear drift across an entire scan, is to chop along the scan direction and force the sum of the differences to equal zero exactly. However, the chop strategy at the JCMT is designed to allow for the Emerson Fourier deconvolution, fixing the chop throws and angles on the sky. This same chop strategy is required for synthetic beam maximum entropy reconstruction. Since the JCMT with the Submillimeter Common-User Bolometer Array (SCUBA) is restricted to scanning along three preferred directions in altitude-azimuth space defined by the hexagonal geometry of the array, the chop direction is usually different from the scan direction. Using the matrix inversion technique, with multiple scan directions and chopping along the scan, will both produce a more intricately connected matrix **C**, which may produce enhanced stability in the reconstruction, and will allow the sum check algorithm to be used for the reduction of baseline offset correlated uncertainty. Tests of various procedures along these lines are underway.

The tests performed have been on clean data with only Gaussian random noise. This is not a complete test of conditions during observations with the JCMT, where sky fluctuations produce correlated noise across bolometers and bolometer gains drift in time. These correlated noises tend to produce excess power at long wavelengths, which is then amplified using either the Emerson or iterative reconstructions. Long-wavelength artifacts may be apparent in the resultant maps. These artifacts are not visible in the synthetic beam maximum entropy reconstruction; however, it is important to note that any *real* structure with long-wavelength modes is also damped using maximum entropy as it tends to be treated as noise in an attempt to produce the *flattest* map possible. This issue is further addressed in the next section.

4. RECONSTRUCTION OF REAL DATA

4.1. *Isolated Source: CRL 618*

To test the capability of the image reconstruction algorithm on real data, the calibration point source CRL 618 was observed at the JCMT. The data for CRL 618 were obtained on 2000 January 26 under excellent conditions, with zenith optical depths at 225 GHz varying slowly from 0.04 to 0.06 (as measured by a tipping radiometer operated by the Caltech Submillimeter Observatory). The pointing was checked on CRL 618 immediately before the observations, and the atmospheric opacity at 850 μm was measured from skydip observations obtained just before and shortly afterward. A series of six 11 arcmin^2 maps was made
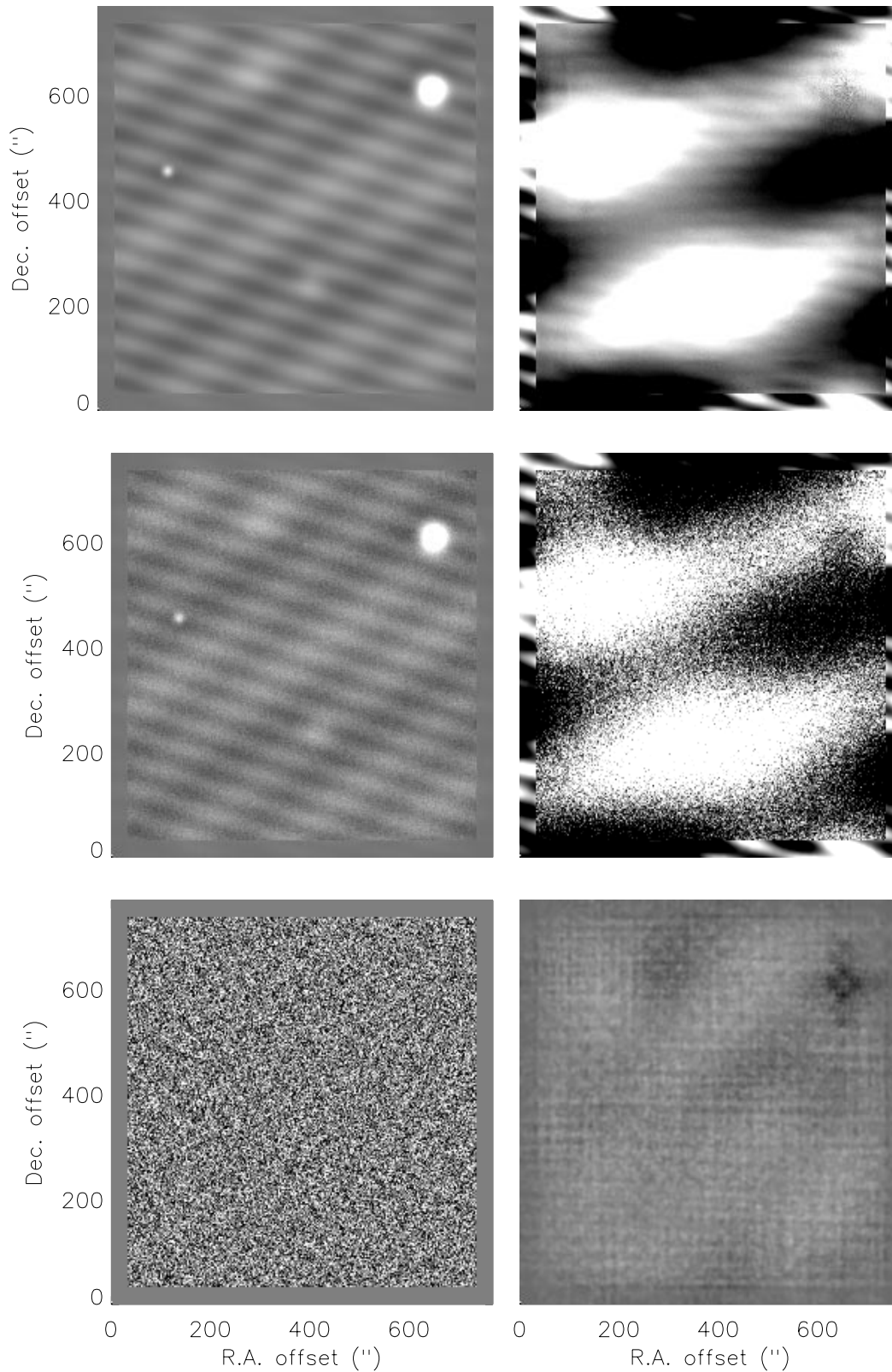
FIG. 6.—Reconstruction of image in Fig. 1 using the maximum entropy inversion technique. *Top row*: Reconstruction from chop maps without noise (*left*) and difference between the reconstructed map and the original artificial map (*right*). *Middle row*: Reconstruction from chop maps with uniform noise (*left*) and difference between the reconstructed map and the original artificial map (*right*). *Bottom row*: Reconstruction from chop maps containing *only* uniform noise and no signal (*left*) and the difference between the sum of the top plus bottom map reconstructions and the middle map reconstruction (*right*). The intensity scales are the same as in Fig. 2.
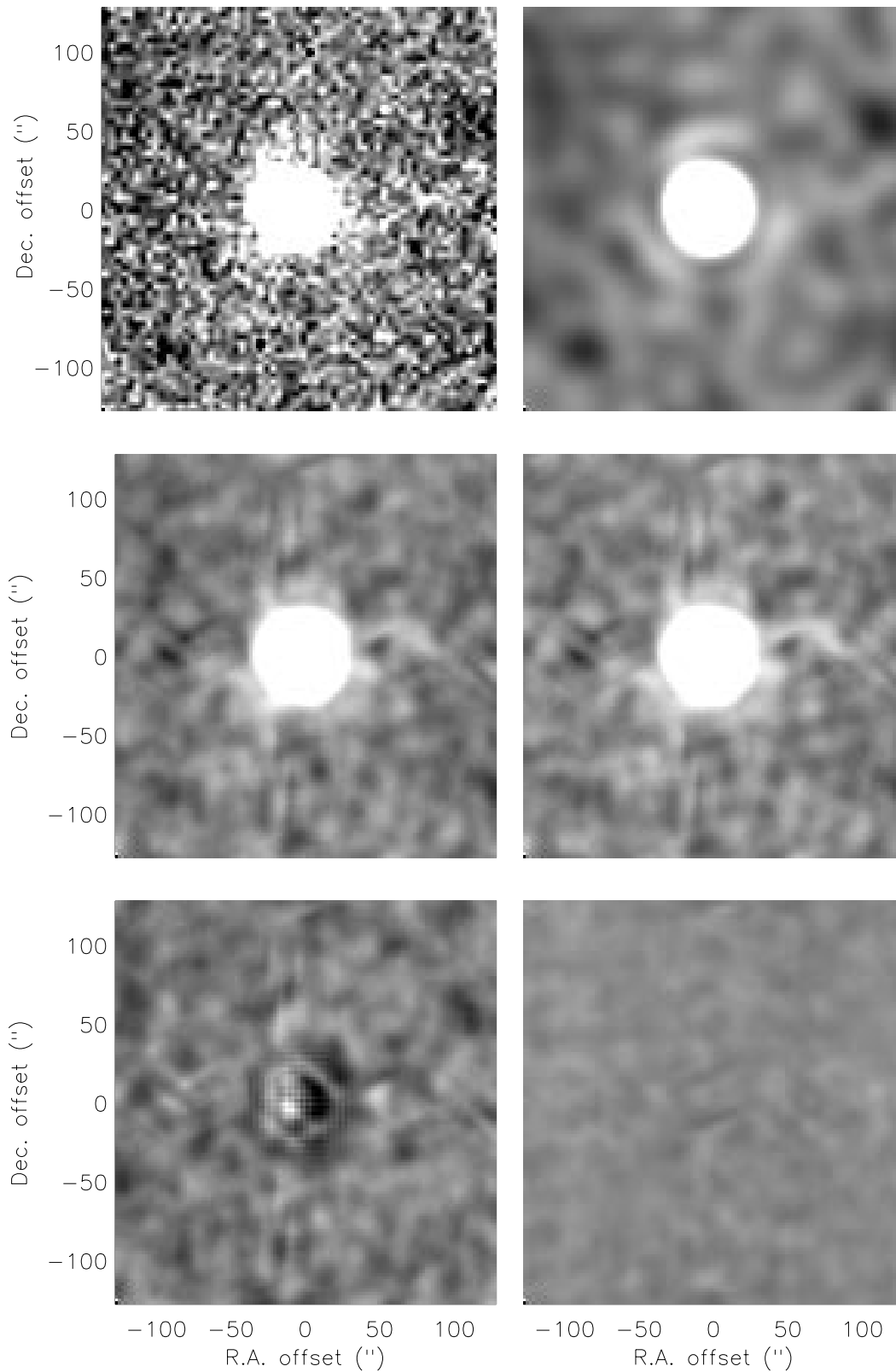
FIG. 7.—Image at 850 μm of CRL 618 obtained with SCUBA at the JCMT and reduced using reconstruction techniques discussed in the text. The intensity scale is linear from -0.2 to 0.2 Jy beam^{-1} to highlight the noise properties of the map. *Top row*: Matrix inversion image reconstruction (*left*) and Wiener-filtered matrix inversion reconstruction (*right*). *Middle row*: Reconstruction using the Emerson Fourier technique (*left*) and the maximum entropy technique (*right*). *Bottom row*: Residual maps after subtracting the Emerson Fourier reconstruction from both the matrix inversion technique (*left*) and the maximum entropy technique (*right*).
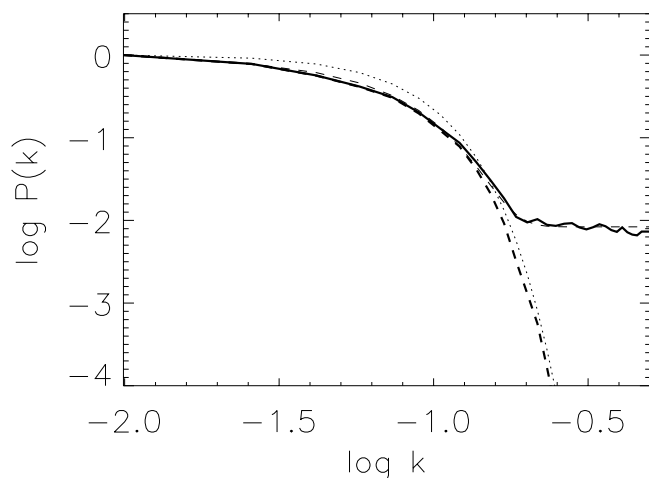
FIG. 8.—Relative power spectrum, in wavenumber k, obtained from a Fourier analysis of the reconstructed image of CRL 618 presented in Fig. 7 (*thick line*). Also plotted are the beam profile power spectrum (*dotted line*), the modeled signal plus noise power spectrum (*dashed line*), and the resultant noise suppressed power spectrum (*thick dashed line*). Note that only large wavenumber or small angular scales are affected by the noise suppression algorithm.

of the object, using chop throws of 30″, 44″, and 68″ oriented in each of right ascension and declination. The scan direction, i.e., the direction in which the array was scanning while chopping, was varied between chop configurations in order to minimize striping. The raw bolometer data were reduced using the standard SCUBA software (Holland et al. 1999) to flat-field and extinction-correct the data.

The data were then further reduced and transformed into the final maps using a variant of the matrix inversion technique discussed in § 2. Three additions to the technique described in § 3 were included in the reconstruction to reduce the effect of correlated uncertainties and residual high-frequency noise. First, the raw bolometer chop data within each map were corrected for any offset baseline introduced during the observations; this complication is usually handled by the standard SCUBA software but has been ported to our private analysis package to allow iterations on the baseline removal. Following T. Jenness (1999, private communication), we treat the baseline as a linear (in time) offset for each bolometer within each scan map, and the initial removal is performed by forcing the sum of all chop measurements with the bolometer to zero. As mentioned in the previous section, this is only a rigorous solution if the chop direction is identical to the scanning direction; however, it is a decent first iteration for the baseline offset and is poor only when the scan crosses a bright region. Further iteration on the baseline is possible during the image reconstruction by searching for correlated differences between the best map produced and the raw bolometer chop data. Second, the correlated noise due to variations across the sky and with time was removed by assuming that at any instant the offset due to the sky was identical for all 37 bolometers and removing the residual fit to the best iterated map. Finally, the raw bolometer noise was computed from the residual variations in the data stream during a given scan map (approximately one thousand chop measurements per bolometer), and this value was used to weight the data. Typically the bolometer noise per measurement for a single scan was $\sigma \sim 0.1$–0.5 Jy, although a few bolometers were considerably noisier. In addition, a

threshold noise level was imposed, which removed all bolometers with $\sigma > 1$ Jy from the data set. Tests were performed to deduce the residual variation in the converged maps using different orderings of the baseline offset and sky noise reduction, and the number of map iterations between offset removals. The residual differences between the maps produced only low-amplitude, long-wavelength modes and no spurious sources.

The results of the matrix inversion image reconstruction are presented in the first panel of Figure 7. Since the noise was added in chop space during the difference measurement, rather than in physical space, this map contains shorter wavelength modes than expected given the 14″ beam size. The input noise, which is spatially uncorrelated, propagates into white noise that includes wavelengths smaller than the beam. Utilizing this information, the data can be optimally filtered using Wiener filtering (Press et al. 1992). In the power spectrum of the map (Fig. 8), the white noise can be treated as a constant power component that is easily identified at high frequencies, where there should be no actual signal due to the finite beam size. The power spectrum component due to the signal is reasonably modeled by multiplying the power spectrum of the beam profile with a power law. (In this analysis, the exact shape of the beam and the power law are not critical; they are required only to allow a smooth transition from noise-dominated high frequencies to signal-dominated low frequencies.) After fitting this two-component model to the spectrum, each Fourier mode is multiplied by the ratio of the strength of the signal to the strength of the noise plus signal. Note that there is no image deconvolution being performed on the map; the beam is not being removed from the data but rather is being used to aid in determining the strength of the signal component compared to the white noise. The second panel of Figure 7 presents the results of Wiener filtering the reconstructed image.

As a further test of the three image reconstruction techniques, the Emerson Fourier reconstruction and the maximum entropy technique were applied to the same data. The standard SCUBA software package was used to remove the correlated noises due to baseline offset and changing sky brightness for this analysis. The results are presented in the middle panels of Figure 7. The angular scale of the residual noise in the middle panels is greater than the raw matrix inversion reduction but smaller than the Wiener-filtered result because the SURF package requires that the chop data be smoothed by $\sim 5''$ before image reconstruction is performed. The bottom panels of Figure 7 show the residuals after subtraction of the Emerson Fourier reconstruction from both the Wiener-filtered matrix inversion reconstruction (*left*) and maximum entropy reconstruction (*right*). Both the maximum entropy technique and Emerson Fourier deconvolution utilize an identical gridding procedure (and the accompanying $\sim 5''$ smoothing) for the chop data before computing the image reconstruction; however, the matrix inversion technique uses the chop data in an independent manner and does not smooth the data prior to reprocessing. Subpixel offsets (in this case ~ 0.3 pixels) result from the different gridding and smoothing procedures and the resulting comparison residual appears slightly asymmetric.

The JCMT beam at 850 μm is nominally 14″; however, the finite scanning rate and the image reconstruction techniques can affect the observed beam size. Before Wiener
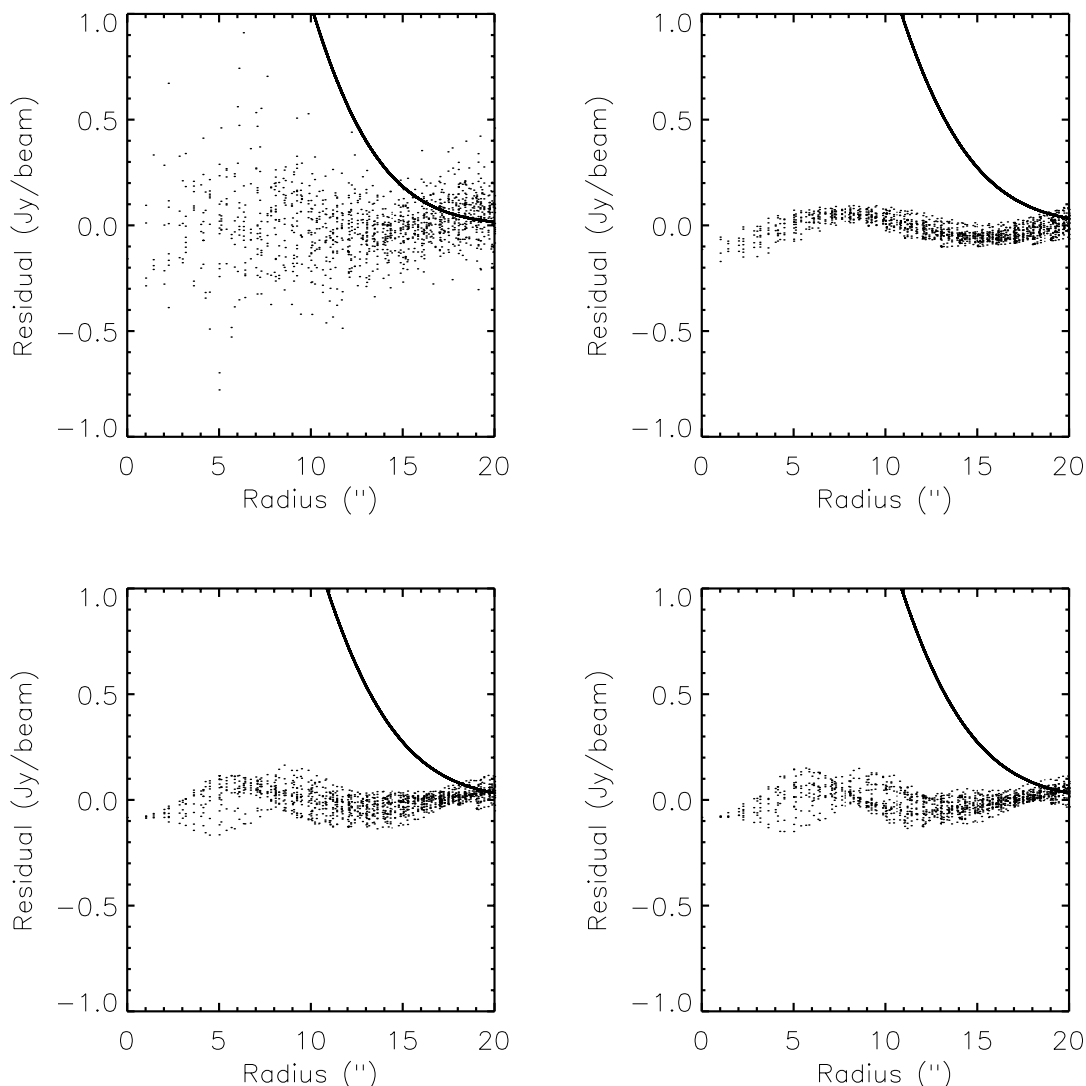
Fig. 9.—Comparison of the residuals after subtracting the best fitting Gaussian beam profile to each of the image reconstruction techniques. The residuals are plotted in distance (arcseconds) from the beam peak. The approximate beam profile is plotted (peak flux 4.2 Jy beam^{-1}) for each technique to allow comparison between the signal and noise levels. *Top row*: Matrix inversion reconstruction residuals (*left*) and Wiener-filtered matrix inversion reconstruction residuals (*right*). *Bottom row*: Emerson Fourier technique residuals (*left*) and maximum entropy technique residuals (*right*).

filtering, the matrix inversion reconstruction, the elliptical beam profile was measured to be 14″2 × 14″0, while after removing the high-frequency components, the beam grew to 15″0 × 14″8. For the Emerson Fourier reconstruction, the elliptical beam shape was measured to be 15″3 × 15″1, and for the maximum entropy technique, the beam shape was 15″1 × 15″3. The residuals between the best-fit beam and the image reconstructions are shown in Figure 9. All three image reconstruction techniques produce a very clean beam profile and thus are well suited for measuring the properties of point sources.

4.2. *Complex Source: ρ Ophiuchi A*

In Paper II, we analyze a 700 arcmin^2 region of the ρ Ophiuchi molecular cloud core. However, here we consider a 100 arcmin^2 subset of the data around the central core, ρ Ophiuchi A, in order to test the map reconstruction algorithm against a complex source. The data for the ρ Ophiuchi region were obtained on 1998 July 10 and 11 and 1999 March 4. These data were also obtained under good to excellent conditions, with zenith optical depths at 225 GHz

0.058 on July 10 and 0.03–0.048 on July 11 and 0.057 on March 4. A skydip observation and pointing check were performed once each hour. Pointing shifts were typically less than 2″. The large mapped region was broken into a series of smaller maps, each approximately 100 arcmin^2. The chop throws used for these maps were 20″, 30″, and 65″ in each of declination and right ascension. The same scan direction was used for all maps, but most of the 100 arcmin^2 regions were observed twice (i.e., with two sets of six chop configurations) at different times of the night so that the orientation of the scan direction in the sky would be different. The data were reduced in the same manner as CRL 618.

The first panel of Figure 10 shows the initial reconstruction, while the second panel shows the reconstruction after Wiener filtering. The map can be compared with the Fourier Emerson reconstruction and maximum entropy technique shown in the middle panels. The linear extensions north and northeast from the ρ Ophiuchi A core are clearly visible in both the matrix inversion images. The three more isolated sources to the east and north are visible in all four maps. The bottom panels of Figure 10 present the result of
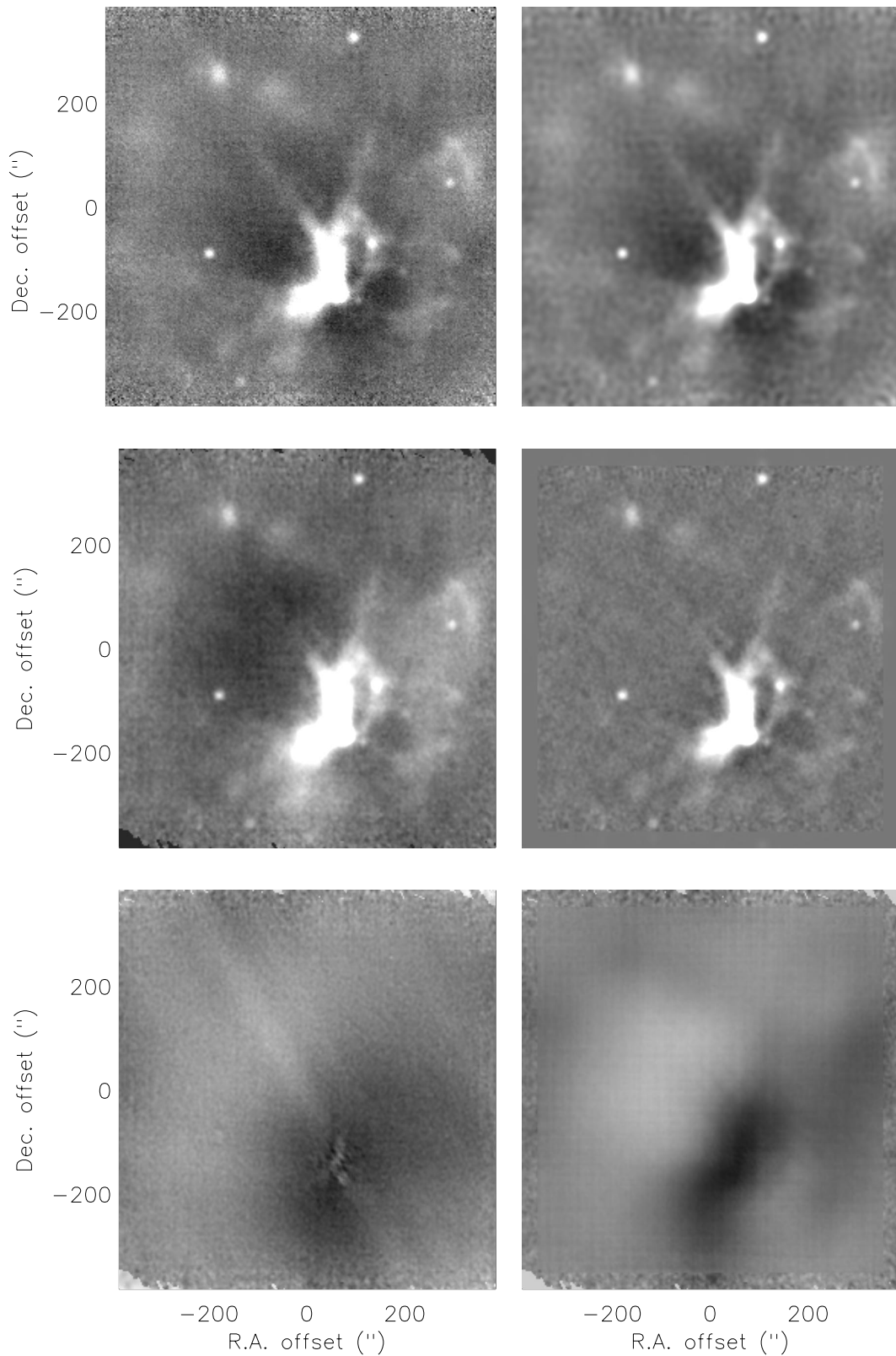
Fig. 10.—Image at 850 μm of the ρ Ophiuchi A core obtained with SCUBA at the JCMT and reduced using reconstruction techniques discussed in the text. The intensity scale is linear from -0.5 to 0.5 Jy beam^{-1} to highlight the noise properties of the map. *Top row*: Matrix inversion image reconstruction (*left*) and Wiener-filtered matrix inversion reconstruction (*right*). *Middle row*: Reconstruction using the Emerson Fourier technique (*left*) and the maximum entropy technique (*right*). *Bottom row*: Residual maps after subtracting the Emerson Fourier reconstruction from both the matrix inversion technique (*left*) and the maximum entropy technique (*right*).

differencing the matrix inversion and Emerson Fourier reconstruction (*left-hand panel*) and the Emerson Fourier reconstruction and maximum entropy technique (*right-hand panel*). In the left-hand panel, significant striping along the scan directions is apparent owing to incomplete removal of the baseline offset in the standard SCUBA software package. By allowing iterations on the baseline removal, the matrix inversion technique is better able to deal with this correlated component. Note that the main scan direction is similar to, but not identical with, the direction of the northeast linear extension, and thus removal of the baseline offset results in a crisper image. As in the reconstruction of CRL 618, slight differences in the gridding of the reconstruction produces artifacts near the center of bright regions. In the bottom right-hand panel, the dominant residuals are the large angular scale modes that the maximum entropy technique is unable to reconstruct (see discussion in § 3). Further analysis of the ρ Ophiuchi molecular cloud, including an analysis of the clump mass function and the two-point correlation function for clump separations, is contained in Paper II.

5. CONCLUSIONS

We have shown that the optimal reconstruction of the sky from two-point chop data involves an iterative approach to matrix inversion. While computationally more demanding than other techniques currently in use, such as maximum entropy and Emerson Fourier deconvolution, the matrix inversion method allows for rigorous calculation of the variance on a pixel by pixel basis and does not require any special observing strategy at the telescope. The data acquisition procedure may be optimized to reduce correlated uncertainties during the observing run, for example, bolometer baseline offset and drift. Tests of different acquisition strategies at the JCMT are now in progress. It should be possible, using the iterative matrix inversion method, to include data taken using different chop procedures such as JCMT jiggle-map data, where a more stable three-point symmetric chop is employed. By combining the effectiveness of scan-mapping large areas, the sensitivity and stability produced in jiggle-maps of specific regions, and the ability to measure effectively the variance at each location within the map, matrix inversion should provide an ideal map reconstruction algorithm for use at the JCMT or any telescope using a chopping strategy.

REFERENCES

Emerson, D. T. 1995, in ASP Conf. Ser. 75, Multi-Feed Systems for Radio Telescopes, ed. D. T. Emerson & J. M. Payne (San Francisco: ASP), 309
Emerson, D. T., Klein, U., & Haslam, C. G. T. 1979, A&A, 76, 92
Holland, W. S., et al. 1999, MNRAS, 303, 659
Jenness, T., & Lightfoot, J. F. 1999, Starlink User Note 216, Starlink Project, CLRC
Jenness, T., Lightfoot, J. F., & Holland, W. S. 1998, in ASP Conf. Ser. 145, Astronomical Data Analysis Software and Systems VII, ed. R. Albrecht, R. N. Hook, & H. A. Bushouse (San Francisco: ASP), 216
Jenness, T., Holland, W. S., Chapin, E., Lightfoot, J. F., & Duncan, W. D. 2000, in ASP Conf. Ser. 216, Astronomical Data Analysis Software and Systems IX, ed. D. Crabtree, N. Manset, & C. Veillet (San Francisco: ASP), in press
Johnstone, D., & Bally, J. 1999, ApJ, 510, L49
Johnstone, D., Wilson, C. D., Moriarty-Schieven, G., Joncas, G., Smith, G., & Fich, M. 2000, ApJ, 545, 327 (Paper II)
Motte, F., André, P., & Neri, R. 1998, A&A, 336, 150
Narayan, R., & Nityananda, R. 1986, ARA&A, 24, 127
Press, W. H., Teukolsky, S. A., Vetterling, W. T., & Flannery, B. P. 1992, Numerical Recipes in C, The Art of Scientific Computing (Cambridge: Cambridge Univ. Press)
Richer, J. S. 1992, MNRAS, 254, 165
Sault, R. J., Teuben, P. J., & Wright, M. C. H. 1995, in ASP Conf. Ser. 77, Astronomical Data Analysis Software and Systems IV, ed. R. A. Shaw, H. E. Payne, & J. J. E. Hayes (San Francisco: ASP), 433
Wilson, C. D., et al. 1999, ApJ, 513, L139
Wright, E. L., Hinshaw, G., & Bennett, C. L. 1996, ApJ, 458, L53